Computational Materials Science 124 (2016) 444–455

Contents lists available at ScienceDirect

Computational Materials Science

journal homepage: www.elsevier.com/locate/commatsci

Numerical analysis of macrosegregation in vertically solidified Pb-Sn test castings – Part I: Columnar solidification

M. Wu [a,b,*], Y. Zheng [a], A. Kharicha [a,b], A. Ludwig [a]

[a] Chair of Modelling and Simulation of Metallurgical Processes, Montanuniversitaet Leoben, Austria
[b] Christian Doppler Lab for Advanced Simulation of Solidification and Melting, Montanuniversitaet Leoben, Austria

ARTICLE INFO

Article history:
Received 22 April 2016
Received in revised form 14 July 2016
Accepted 16 July 2016
Available online 6 August 2016

Keywords:
Macrosegregation
Columnar solidification
Thermo-solutal convection

ABSTRACT

Macrosegregation in a casting is caused by different flow and crystal movement phenomena during solidification. In order to get basic understanding of the macrosegregation mechanisms, 8 simple test cases of a 2D casting ($50 \times 60\ \mathrm{mm}^2$) with unidirectional cooling from either top or bottom were configured and calculated by using a volume-average based three-phase solidification model (Wu and Ludwig, 2006). Two different alloys were considered: Sn-10 wt.%Pb with solute element Pb heavier than the solvent Sn; Pb-18 wt.%Sn with solute element Sn lighter than the solvent Pb. The work is presented in two parts. Part I (this paper) presents 4 cases of pure columnar solidification. Direction of the thermal-solutal buoyancy force of the interdendritic melt can be estimated according to the alloy (Sn-10 wt.%Pb or Pb-18 wt.% Sn); and the possible flow pattern can also be estimated when the solidification direction (upwards or downwards) is known. As consequence, the macrosegregation tendency should be estimated as well. However, the modelling results show that complicated details of macrosegregation distribution can develop due to the complexity of the transient flow. Other 4 cases of equiaxed solidification will be presented as Part II in next paper.

1. Introduction

Understanding the formation of macrosegregation in castings has been, and it remains to be, an important topic in the solidification researches [1,2]. It is also one of the key topics in the annual “solidification course”, as held in Les Diablerets, Swiss Federal Institute of Technology of Lausanne (EPFL), Switzerland. The one-week course is designed for engineers and scientists who wish to improve their knowledge in the field of solidification. 8 simple test cases of a 2D casting with unidirectional cooling from either top or bottom, as shown in Fig. 1 [3,4], were taken as exercises for the course-participants to test their knowledge about macrosegregation. In principle, if the directions of buoyancy force and crystal sedimentation are known, one can estimate the possible macrosegregation tendency. The current work is to simulate these 8 cases numerically. One purpose is to confirm the knowledge. A more important purpose is to demonstrate the potential complexity of the macrosegregation phenomena. Macrosegregation occurring in these simple test cases are sometimes beyond the knowledge.

Macrosegregation is mainly caused by different melt flow [1,2,5–9] and crystal sedimentation [10–13] phenomena. In some cases the solid dendrite deformation in the mush region [6,14], the exudation of interdendritic melt close to the casting surface [15,16], and even the macroscopic solute diffusion in the interdendritic melt can also cause macrosegregation [17,18]. The macroscopic diffusion induced macrosegregation is very weak [19]. In order to simulate macrosegregation different solidification models by considering the above multiphase transport phenomena were developed. The continuum model [20–24] was the earliest one. It treats the mushy zone as a solid-liquid mixture, and conservation equations (mass, momentum, energy and species) for both liquid and solid phases are merged to form a set of mixture conservation equations, i.e. the concerned liquid and solid phases are simplified as one phase mixture. In the early 1990s the group of Beckermann developed multiphase solidification models based on Eulerian-Eulerian volume-average approach [10,25,26]. Conservation of mass, momentum, energy and species for each phase (liquid, equiaxed and/or columnar) are considered separately. Interactions between the phases are treated and the conservation equations are solved in a coupled manner. This work was recently extended by Wu et al. [11,12,27–38] and Leriche et al. [39]. A series of multiphase volume-average solidification models were proposed.

---

* Corresponding author at: Chair of Modelling and Simulation of Metallurgical Processes, Montanuniversitaet Leoben, Austria.

E-mail address: menghuai.wu@unileoben.ac.at (M. Wu).

http://dx.doi.org/10.1016/j.commatsci.2016.07.017
0927-0256/

Nomenclature

c_0	initial concentration, (1)
c_ℓ, c_c	species concentration, (1)
c^{ref}	reference concentration, (1)
c_{eu}	eutectic concentration, (1)
c_ℓ^*, c_c^*	equilibrium concentration at interface, (1)
$C_{\ell c}^{p}$	species exchange between liquid and columnar, ($\mathrm{kg \cdot m^{-3} \cdot s^{-1}}$)
c^{index}	macrosegregation index, (%)
c_{mix}	mix concentration, (1)
c_p^ℓ, c_p^c	specific heat, ($\mathrm{J \cdot kg^{-1} \cdot K^{-1}}$)
D_ℓ, D_c	diffusion coefficient, ($\mathrm{m^2 \cdot s^{-1}}$)
d_c	columnar trunk diameter, (m)
f_ℓ, f_c	volume fraction of different phases, (1)
$\vec{g}$	gravity, ($\mathrm{m \cdot s^{-2}}$)
$\vec{g}'_\ell$	reduced gravity, ($\mathrm{m \cdot s^{-2}}$)
h	heat transfer coefficient, ($\mathrm{W \cdot m^{-2} \cdot K^{-1}}$)
H^*	volume heat transfer coefficient between phases, ($\mathrm{W \cdot m^{-3} \cdot K^{-1}}$)
h_ℓ, h_c	enthalpy, ($\mathrm{J \cdot kg^{-1}}$)
h_ℓ^{ref}, h_c^{ref}	reference enthalpy, ($\mathrm{J \cdot kg^{-1}}$)
Δh	latent heat, ($\mathrm{J \cdot kg^{-1}}$)
K	permeability of liquid in porous medium, ($\mathrm{m^2}$)
k	solute partitioning coefficient at the liquid solid interface, (1)
k_ℓ, k_c	thermal conductivity, ($\mathrm{W \cdot m^{-1} \cdot K^{-1}}$)
l	actual columnar length in tip cell, (m)
$M_{\ell c}(= -M_{c\ell})$	liquid-columnar net mass transfer rate, ($\mathrm{kg \cdot m^{-3} \cdot s^{-1}}$)
m	slope of liquidus in phase diagram, (K)
p	pressure, ($\mathrm{N \cdot m^{-2}}$)
$Q_{\ell c}(= -Q_{c\ell})$	total energy exchange between liquid and columnar phases, ($\mathrm{J \cdot m^{-3} \cdot s^{-1}}$)
$Q_{\ell c}^{d}(= -Q_{c\ell}^{d})$	energy transfer between liquid and columnar phases, ($\mathrm{J \cdot m^{-3} \cdot s^{-1}}$)
$Q_{\ell c}^{p}(= -Q_{c\ell}^{p})$	energy exchange due to phase change between liquid and columnar phases, ($\mathrm{J \cdot m^{-3} \cdot s^{-1}}$)
R_{tip}	primary dendrite tip radius, (m)

R_c	columnar radius, (m)
$R_{f,c}$	maximum radius of columnar trunk, (m)
T_0	initial temperature, (K)
T, T_ℓ, T_c	temperature, (K)
T_f	melting point of solvent at $c_0 = 0$, (K)
T_{ref}	reference temperature for enthalpy definition, (K)
T_{eu}	eutectic temperature, (K)
T_{liq}	liquidus temperature, (K)
T_{EXT}	external temperature, (K)
ΔT	constitutional undercooling, (K)
t	time, (s)
Δt	time step, (s)
$\vec{U}_{\ell c}(= -\vec{U}_{c\ell})$	total liquid-columnar momentum exchange rate, ($\mathrm{kg\ m^{-2} s^{-2}}$)
$\vec{U}_{\ell c}^{d}(= -\vec{U}_{c\ell}^{d})$	liquid-columnar momentum change due to drag force, ($\mathrm{kg \cdot m^{-2} \cdot s^{-2}}$)
$\vec{U}_{\ell c}^{p}(= -\vec{U}_{c\ell}^{p})$	liquid-columnar momentum exchange due to phase change, ($\mathrm{kg \cdot m^{-2} \cdot s^{-2}}$)
$\vec{u}_\ell$	velocity vector, ($\mathrm{m \cdot s^{-1}}$)
v_{Rc}	growth speed in radius direction for columnar, ($\mathrm{m \cdot s^{-1}}$)
v_{tip}	growth speed in tip direction, ($\mathrm{m \cdot s^{-1}}$)
V_{domain}	volume of the calculated domain, ($\mathrm{m^3}$)
β_T	thermal expansion coefficient, ($\mathrm{K^{-1}}$)
β_c	solutal expansion coefficient, (1)
Γ	Gibbs Thomson coefficient, ($\mathrm{m \cdot K}$)
λ_1	primary columnar arm space, (m)
μ_ℓ	viscosity, ($\mathrm{kg \cdot m^{-1} \cdot s^{-1}}$)
ρ_ℓ, ρ_c	density, ($\mathrm{kg \cdot m^{-3}}$)
ρ_{ref}	reference density, ($\mathrm{kg \cdot m^{-3}}$)
ρ_ℓ^{b}	density for buoyancy force, ($\mathrm{kg \cdot m^{-3}}$)
$\bar{\bar{\tau}}_\ell$	stress-strain tensors, ($\mathrm{kg \cdot m^{-1} \cdot s^{-1}}$)

Subscripts

ℓ	mark liquid
c	columnar phases

The numerical model used for the current work is based on a three phase mixed columnar-equiaxed solidification model as developed by Wu and Ludwig [28,29,37,38]. Conception of test cases of Fig. 1 comes from the exercises of the "solidification course" at EPFL [3,4]. The geometry, alloys and most of material properties are taken from a numerical benchmark as suggested by Bellet et al. [40], but the thermal boundary conditions are set differently. The test cases of Fig. 1 are cooled either from bottom or from top, while the benchmark of the Ref. [40] is cooled from a side wall. Studies, based on the similar benchmark as cooled from a side wall, are many, both numerically [35,36,41,42] and experimentally [43,44], but they focused on the formation of channel segregation. The simple design of the test cases (Fig. 1) is to minimize the complexity of macrosegregation for a learning purpose. The current work is presented in two parts. Part I (this paper) presents the 4 cases of pure columnar solidification. The other 4 cases of equiaxed solidification will be presented as Part II in next paper.

2. Numerical model and simulation settings

Model details can be found in previous publications [28,29,37,38]. Here, only two phases, liquid and columnar, are considered. The functionalities of the model for the nucleation and growth of equiaxed phase are "switched off". A brief outline of the model and main assumptions are described below. Conservation equations, source and exchange terms, and some auxiliary equations are summarized in Table 1.

(1) The two phases are the liquid melt and the solid columnar dendrite trunks.
(2) The morphology of the columnar dendrite trunks is approximated by step-wise growing cylinders positioned in a staggered arrangement with constant primary dendritic arm spacing, λ_1.
(3) The columnar trunks grow from the casting surface when constitutional undercooling develops and the columnar tip is tracked applying the LGK model [45,46].
(4) The liquid-to-solid mass transfer (solidification/melting) rate, $M_{\ell c}$, is calculated as a function of the growth velocity of the columnar trunks, v_{R_c}, which is governed by diffusion of the solute in the interdendritic melt around each cylindrical trunk.
(5) Thermodynamic equilibrium is assumed at the liquid-solid interface, which determines the interface concentrations (c_ℓ^*, c_c^*). Back diffusion in solid is neglected ($D_c = 0$). The concentration difference ($c_\ell^* - c_\ell$) is the driving force for the growth of columnar trunks.

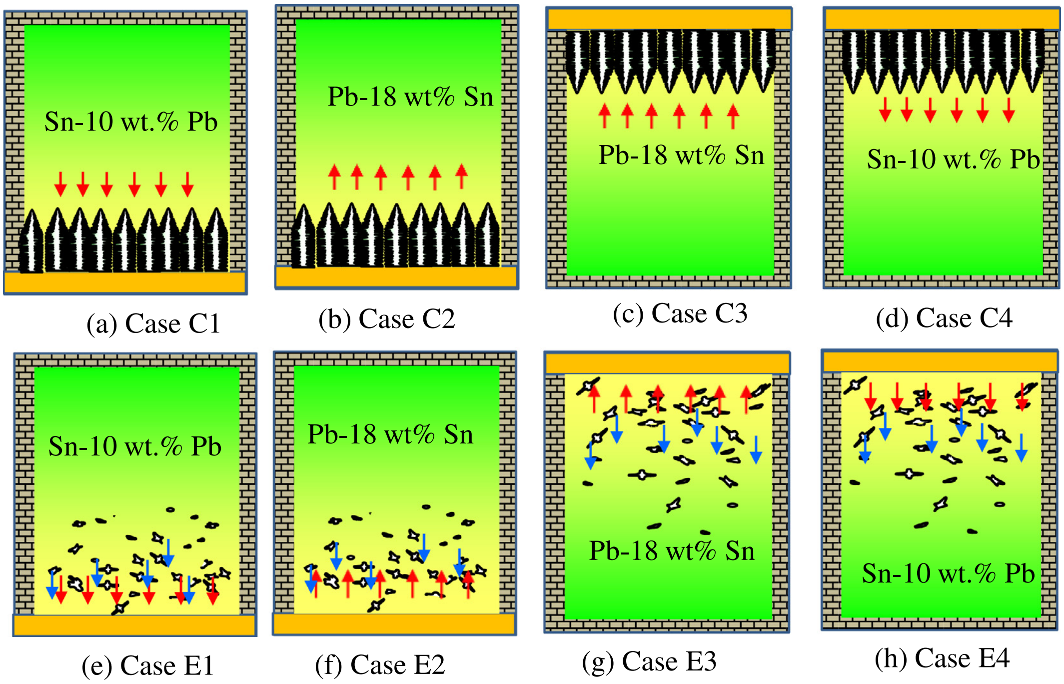

Fig. 1. Schematics of columnar (upper row) and equiaxed (lower row) solidification, solutal buoyancy force direction (red arrows) of the interdendritic/intergranular melt, and crystal sedimentation direction (blue arrows) of the equiaxed grains. 8 cases are defined. Two different alloys were considered: Sn-10 wt.%Pb with solute element Pb heavier than the solvent Sn; Pb-18 wt.%Sn with solute element Sn lighter than the solvent Pb. Color gradient indicates the distribution of solute element in the melt: yellow for enrichment, green as the nominal composition. The yellow walls indicate chilled walls, while the hatched ones are adiabatic. Cases C1, C2, E1 and E2 are cooled from bottom, while other 4 cases are cooled from top. (For interpretation of the references to color in this figure legend, the reader is referred to the web version of this article.)

(6) Volume-averaged concentrations for each phase (c_ℓ, c_c) are solved by global species conservation equations. A macrosegregation index (c^{index}) based on the phase-mixture concentration (c_{mix}) is defined by Eqs. (14) and (15). The quantity of c^{index} is presented in %. Additionally, a global macrosegregation intensity (GMI) is defined by Eq. (16) to evaluate the global segregation severity.

(7) A linearized binary Sn-Pb phase diagram with a constant solute partitioning coefficient k and a constant liquidus slope m is used.

(8) Interdendritic flow resistance in the mushy zone is calculated via a permeability law according to the Blake-Kozeny approach [47].

(9) Solidification shrinkage is not accounted for and we assume $\rho_\ell = \rho_c$. Thermo-solutal convection of the liquid melt is modelled with the Boussinesq approximation. The solid columnar phase is considered to be rigid and stationary.

The configuration of the test cases in 2D is shown in Fig. 2. The geometry, alloys and most of material properties are taken from a numerical benchmark as suggested by Bellet et al. [40]. Only half of the casting domain is calculated by setting a symmetry plane at the left boundary. Two different alloys (Fig. 3) were considered: one is Sn-10 wt.%Pb with solute element Pb heavier than the solvent Sn; the other is Pb-18 wt.%Sn with solute element Sn lighter than the solvent Pb. The materials chosen for these simulations have advantages of relatively simple phase diagram and well known properties, as well as a large temperature interval in the two-phase region during solidification and a large density difference between components. Both of the latter two characteristics enhance macrosegregation [19]. Thermodynamic data and thermal physical properties of both alloys are available, as listed in Table 2. The benchmark is cooled unidirectionally, either from bottom or from top. Therefore, 4 cases of calculations are defined and they are correspondent to the 4 cases in the upper row of Fig. 1.

The model is implemented in ANSYS FLUENT, version 14.5 [51]. Although FLUENT formulation is implicit and theoretically there is no stability criterion to be met in determining the time step Δt, the time steps used impact the accuracy of the numerical results. Due to the complexity of the coupling, there is no formulation to determine the optimal Δt. For each time step, 60 iterations are adopted to decrease the scaled residual of concentration, flow quantities and pressure below 10^{-4} and enthalpy quantities below 10^{-7}. The scaled residual [51] is the sum of the imbalance in the discretized conservation equations over all computational cells (volume elements), $\sum_{\text{cells,P}}|\sum_{\text{nb}} a_{\text{nb}}\phi_{\text{nb}} + b - a_{\text{P}}\phi_{\text{P}}|$, being normalized by a scaling factor, $\sum_{\text{cells,P}}|a_{\text{P}}\phi_{\text{P}}|$. Here ϕ_{P} and ϕ_{nb} are values of a general variable ϕ at a cell P and neighbor cells nb, a_{P} is the center coefficient, a_{nb} are the influence coefficients for the neighboring cells, and b is the contribution of the constant part of the source term. Mesh size is 10^{-3} m, and initial Δt is 10^{-3} s. In order to enhance the calculation efficiency, Δt can be gradually and manually increased to 0.01 s during the late stage of solidification. One case simulation takes 2 days to complete on a high performance cluster (2.6 GHz, 8 Cores).

3. Modelling results

3.1. Case C1

This case (Fig. 1(a)) considers the solidification of Sn-10 wt.%Pb alloy from the bottom. A solidification sequence, as indicated by isolines of f_c, and the evolution of macrosegregation (c^{index}) in color are shown in Fig. 4. The solidification progresses smoothly and unidirectionally. Both the thermal and solutal buoyancy forces of the liquid melt act in the direction against the solidification direction, hence no flow occurs. However, a very weak macrosegregation still occurs at the bottom and top surface. At the bottom the maximum negative segregation (c^{index}) is −3.5%, while at the top positive

Table 1
Conservation equations, source and exchange terms, auxiliary equations.

Conservation equations			
Mass	$\frac{\partial}{\partial t}(f_\ell \rho_\ell) + \nabla \cdot (f_\ell \rho_\ell \vec{u}_\ell) = -M_{\ell c}$ $\frac{\partial}{\partial t}(f_c \rho_c) = M_{\ell c}$		(1)
Momentum	$\frac{\partial}{\partial t}(f_\ell \rho_\ell \vec{u}_\ell) + \nabla \cdot (f_\ell \rho_\ell \vec{u}_\ell \otimes \vec{u}_\ell) = -f_\ell \nabla p + \nabla \cdot \bar{\bar{\tau}}_\ell + f_\ell \rho_\ell \vec{g}'_\ell - \vec{U}_{\ell c}$ with $\vec{g}'_\ell = \frac{\rho_\ell^b(T,c) - \rho_\ell}{\rho_\ell} \vec{g}$, $\rho_\ell^b(T,c) = \rho_\ell \cdot [1 + \beta_T \cdot (T^{ref} - T_\ell) + \beta_c \cdot (c^{ref} - c_\ell)]$, where $\vec{U}_{\ell c} = \vec{U}_{\ell c}^p + \vec{U}_{\ell c}^d$		(2)
Species	$\frac{\partial}{\partial t}(f_\ell \rho_\ell c_\ell) + \nabla \cdot (f_\ell \rho_\ell \vec{u}_\ell c_\ell) = \nabla \cdot (f_\ell \rho_\ell D_\ell \nabla c_\ell) - C_{\ell c}^p$ $\frac{\partial}{\partial t}(f_c \rho_c c_c) = \nabla \cdot (f_c \rho_c D_c \nabla c_\ell) + C_{\ell c}^p$		(3)
Enthalpy	$\frac{\partial}{\partial t}(f_\ell \rho_\ell h_\ell) + \nabla \cdot (f_\ell \rho_\ell \vec{u}_\ell h_\ell) = \nabla \cdot (f_\ell k_\ell \nabla \cdot T_\ell) - Q_{\ell c}$ $\frac{\partial}{\partial t}(f_c \rho_c h_c) = \nabla \cdot (f_c k_c \nabla \cdot T_c) + Q_{\ell c}$ with $Q_{\ell c} = Q_{\ell c}^p + Q_{\ell c}^d$, $h_\ell = \int_{T_{ref}}^{T_\ell} c_p^\ell dT + h_\ell^{ref}$, $h_c = \int_{T_{ref}}^{T_e} c_p^c dT + h_c^{ref}$, $L = h_\ell^{ref} - h_c^{ref}$		(4)
Solidification net mass transfer			
Mass transfer	$M_{\ell c} = v_{R_c} \cdot S_A \cdot \rho_c \cdot \Phi_{imp}$ for trunks $M_{\ell c} = v_{R_c} \cdot n_c \cdot (\pi d_c \cdot l) \cdot \rho_\ell \cdot \Phi_{imp} + v_{tip} \cdot n_c \cdot (\pi R_{tip}^2) \cdot \rho_\ell \cdot \Phi_{imp}$ for trunks incl. col. tip		(5)
Col. trunk growth velocity	$v_{R_c} = \frac{dR_c}{dt} = \frac{D_\ell}{R_c} \cdot \frac{(c_\ell^* - c_\ell)}{(c_\ell^* - c_c^*)} \cdot \ln^{-1}\left(\frac{R_{f,c}}{R_c}\right)$		(6)
Diameter of col. trunks	$d_c (= 2R_c) = \lambda_1 \cdot \sqrt{\frac{\sqrt{12} \cdot f_c}{\pi}}$		(7)
Far field radius of col. trunks	$R_f = \frac{1}{\sqrt{3}} \cdot \lambda_1$		(8)
Col. surface concentration	$S_A = \frac{d_c \cdot \pi}{\lambda_1^2}$		(9)
Growing surface impingement	$\Phi_{imp} = \begin{cases} 1 & d_c \leqslant \lambda_1 \\ 2\sqrt{3} \cdot f_\ell / (2\sqrt{3} - \pi) & d_c > \lambda_1 \end{cases}$		(10)
Source and exchange terms			
Momentum transfer	$\vec{U}_{\ell c}^p = \vec{u}_\ell \cdot M_{\ell c}$	$\vec{U}_{\ell c}^d = \frac{f_\ell^2 \cdot \mu_\ell}{K} \cdot \vec{u}_\ell$ where $K = 6 \times 10^{-4} \cdot \lambda_1^2 \cdot \frac{f_\ell^3}{(1 - f_\ell)^2}$	(11)
Species transfer	$C_{\ell c}^p = k \cdot c_\ell^* \cdot M_{\ell c}$		(12)
Enthalpy transfer and latent heat	$Q_{\ell c}^p = h_\ell \cdot M_{\ell c}$	$Q_{\ell c}^d = H^* \cdot (T_\ell - T_c)$ where $H^* = 10^9$ W m^{-2} K^{-1}	(13)
Auxiliary equation			
Mixture concentration	$c_{mix} = (c_\ell \cdot \rho_\ell \cdot f_\ell + c_c \cdot \rho_c \cdot f_c)/(\rho_\ell \cdot f_\ell + \rho_c \cdot f_c)$		(14)
Macrosegregation index	$c^{index} = \frac{c_{mix} - c_0}{c_0} \times 100$		(15)
Global macroseg. intensity (GMI)	$\mathrm{GMI} = \frac{1}{V_{domain}} \cdot \iiint_{V_{domain}} \lvert c^{index} \rvert dV$		(16)

segregation (c^{index}) reaches a maximum of 0.64%. The reason for this is due to macroscopic interdendritic solute diffusion. As the schematic (insert) of Fig. 1(a) shows, the interdendritic melt is enriched with solute element (Pb), and there exists a relatively strong concentration gradient in the mushy zone. This solute concentration gradient invokes solute diffusion from the surface towards inner regions, causing a mini layer of negative segregation at the bottom surface where solidification starts. The same mechanism operates at the end of solidification when the solidification front reaches the top surface, and the solute diffusion towards the top surface leads to the formation of a positive segregation layer there. In order to prove this hypothesis an additional numerical calculation is made for the same case C1, but the solute diffusion coefficient is intentionally chosen as a very small value, $D_\ell = 1.0 \times 10^{20} \mathrm{m}^2 \cdot \mathrm{s}^{-1}$, instead of the physical value of $4.5 \times 10^{-9} \mathrm{m}^2 \cdot \mathrm{s}^{-1}$. As expected these mini surface segregation layers vanish.

This segregation mechanism was firstly reported by Schneider and Beckermann [17], and further verified by Thevik and Mo [18]. The surface segregation layer is extremely narrow, in a magnitude of 100 μm, and the segregation in this layer is very weak. If other flow mechanisms, e.g. shrinkage induced flow and thermo-solutal convection, are involved, this macroscopic diffusion induced surface segregation will be easily overwelmed by other flow effects [19].

3.2. Case C2

This case (Fig. 1(b)) considers an alloy of Pb-18 wt.%Sn, where the solute element Sn is lighter than the solvent Pb. Although thermal buoyancy is always in the same direction as gravity, i.e. against the solidification direction to keep the melt in the mushy zone, the solute enriched interdendritic melt tends to rise, and provokes melt flow. The solutal buoyancy overweighs the thermal buoyancy when solidification starts. A solidification sequence, with melt flow and induced macrosegregation are shown in Fig. 5. Although the global solidification sequence is unidirectional, the temperature field and the contour of fraction solid f_c are obviously disturbed by the flow. The flow pattern is very transient, some vortex develops dynamically. The flow velocities are in the order of 10^{-3} m/s, but it can reach a maximum of 10^{-2} m/s occationally. This kind of flow pattern continuously brings solute enriched melt out of the interdendritic region, and mixed with bulk melt. The bulk melt in the upper part is gradually enriched with the solute, and it leads to the formation of a large positive segregation zone in the upper region. As balance, a large negative segregation zone forms in the lower part. At 300 s, the local macrosegregation index falls in a range of −39.0 to 62.0%. This range is adapted to −38.0 to 124.0% at the end of solidification. The diffusion induced surface segregation at the top and bottom surfaces should occur as well, but its

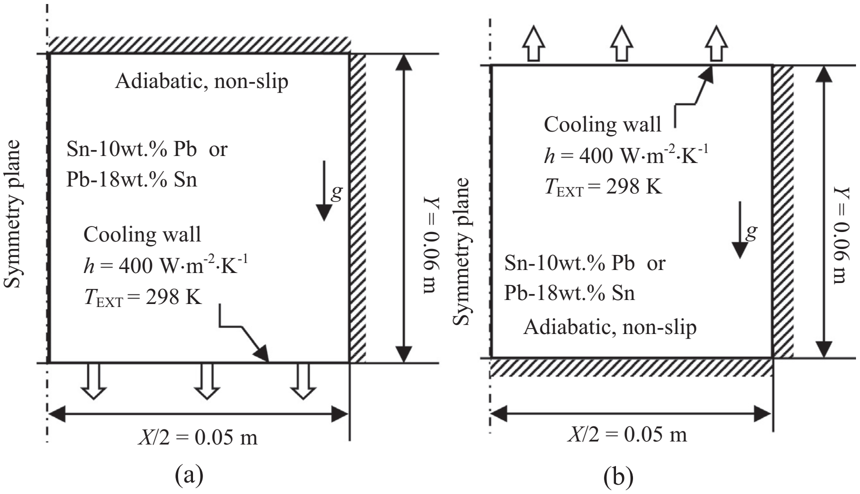

Fig. 2. Geometry of test cases with boundary and initial conditions.

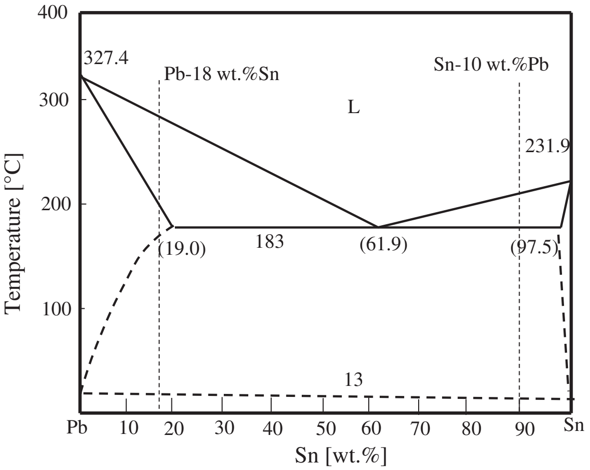

Fig. 3. Phase diagram of Pb-Sn binary alloy system.

magnitude is so small that it is almost undetectable in the presence of convection-induced segregation.

One interesting phenomenon is that positive segregation channels are developed along both side boundaries, i.e. symmetry plane (left) and adiabatic and non-slop wall (right). The segregation intensity and patterns along both left and right boundaries are similar. The symmetry plane here is actually consistent with an adiabatic and free-slip wall. It seems that non-slip and free-slip boundary conditions play a similar role. By analyzing the flow fields of Fig. 5(c.1)–(c.4), we find that the flow pattern is largely confined by the domain boundaries. The interdendritic melt near the side boundaries is difficult to be brought out of the mushy region, and the solidification is retarded, hence channels form there.

It is observed that the dynamic flow pattern tends to build some local compositional heterogeneity (strip-like structure, or mini channel segregates) in the inner part of the benchmark, as seen in Fig. 5(d.1)–(d.4). Those segregation structures are not stable, and they survive only temporarily. Depending on the change of

Table 2
Material properties and other parameters.

	Symbol	Units	Sn-10 wt.%Pb	Pb-18 wt.%Sn	Ref.
Nominal concentration	c_0	–	10.0 wt.% Pb	18.0 wt.% Sn	
Liquidus temperature	T_{liq}	K	492.14	558.63	[40]
Melting point of solvent at $c_0 = 0$	T_{f}	K	505	600.65	[40]
Eutectic composition	c_{eu}	wt.%	38.1	61.9	[40]
Eutectic temperature	T_{eu}	K	456	456	[41]
Liquidus slope	m	K (wt.%)$^{-1}$	−1.286	−2.334	[40]
Equilibrium partition coefficient	k	–	0.0656	0.310	[40]
Reference density	ρ_{ref}	kg·m^{-3}	7000	9250	[40]
Specific heat	c_{p}^{ℓ}, $c_{\mathrm{p}}^{\mathrm{c}}$	J·kg^{-1}·K^{-1}	260	176	[40]
Thermal conductivity	k_ℓ, k_c	W·m^{-1}·K^{-1}	55.0	17.9	[40]
Latent heat	Δh_{f}	J·kg^{-1}	6.1×10^4	3.76×10^4	[40]
Viscosity	μ_ℓ	kg·m^{-1} s^{-1}	1.0×10^{-3}	1.1×10^{-3}	[40]
Liquid thermal expansion coefficient	β_{T}	K^{-1}	6.0×10^{-5}	1.16×10^{-4}	[40]
Liquid solutal expansion coefficient	β_{C}	wt.%$^{-1}$	-5.3×10^{-3}	4.9×10^{-3}	[40]
Primary dendritic arm spacing	λ_1	m	1.3×10^{-3}	1.85×10^{-3}	[40]
Diffusion coefficient (solid)	D_c	m^2·s^{-1}	1.0×10^{-12}	1.0×10^{-12}	[48]
Diffusion coefficient (liquid)	D_ℓ	m^2·s^{-1}	4.5×10^{-9}	4.5×10^{-9}	[48]
Initial temperature	$T_0 = \mathrm{T}_{\mathrm{liq}}$	K	492.14	558.64	[40]
Heat transfer coefficient	h	W·m^{-2}·K^{-1}	400	400	[40]
External temperature	T_{EXT}	K	298	298	[40]
Density difference of solid and liquid	$\Delta\rho$	kg·m^{-3}	304	420	[49]
Gibbs Thomson coefficient	Γ	m·K	6.5×10^{-8}	7.9×10^{-8}	[50]

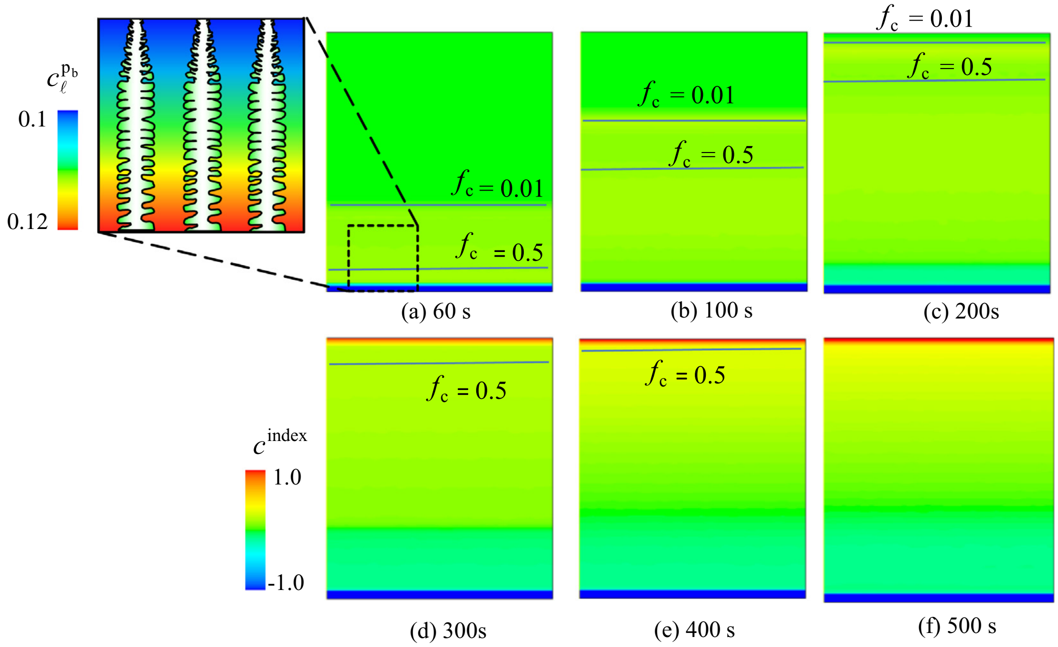

(a) 60 s (b) 100 s (c) 200s

(d) 300s (e) 400 s (f) 500 s

Fig. 4. Solidification process and macrosegregation evolution of Case C1. The contour of c^{index} (%) in color scale is overlaied with isolines $f_\ell = 0.99$ and $f_\ell = 0.5$. Alloy is Sn-10 wt.%Pb. Columnar tip front position is represented by $f_c = 0.01$. (For interpretation of the references to color in this figure legend, the reader is referred to the web version of this article.)

local flow direction, some structures appear while some others vanish. Consequence of this dynamics is that a non-uniform c^{index} distribution develops.

3.3. Case C3

In this case (Fig. 1(c)) we consider Pb-18 wt.%Sn alloy, which is unidirectionally cooled from the top. As shown in Fig. 6, solidification starts from the top surface and the solidification front moves downwards. Thermal buoyancy drives the flow initially downwards, while solute (lighter) buoyancy is in the direction against the solidification direction and tends to stabilize the flow. Although the solute buoyancy overweighs the thermal buoyancy, there still exists a weak flow (magnitude of 10^{-5} m/s) in the bulk region. At the beginning of cooling before solidification starts, the thermal buoyancy flow reaches its maximum of 10^{-3} m/s, but this flow is to a great extent suppressed by solutal buoyancy as solidification begins. Obviously, the weak flow disturbs the solidification front slightly, and it can induce a quite special pattern of macrosegregation. In the center part a positive segregation region develops, while at the right side and left side of this area depletion in solutal element and negative macrosegregation occur. The final macrosegregation intensity falls in the range of −3.96 to 1.34%, i.e. the similar range of case C1 (diffusion induced surface segregation). As shown in Fig. 6(d.1)–(d.4), a diffusion-induced negative segregation layer at the top surface and a diffusion-induced positive segregation layer at the bottom are detectable, and they are in the same range of the weak flow-induced segregation.

3.4. Case C4

In Case C4 (Fig. 1(d)) we consider an alloy of Sn-10 wt.%Pb, which cooled from the top. This case is actually quite similar to case C2, just solidifies in the opposite direction. As shown in Fig. 7, both thermal and solutal buoyancy operate in the same direction, driving the flow. Therefore, the final segregation (c^{index}) range, from −58 to 156%, is stronger than the case C2. The dynamics of flow for both cases are not identical, but similar. The final segregation distribution patterns are quite similar as well. For the analysis of case C4 we can refer to Case C2.

4. Discussion

4.1. Macrosegregation intensity by different mechanisms

Calculated macrosegregation results of 4 cases are compared in Fig. 8. The segregation distribution is shown in color scale, but its intensity is analyzed by the c^{index} distribution range as labelled in the figures and by the so-called global macrosegregation intensity (GMI). GMI, as defined by Eq. (16), is used to evaluate the global average segregation intensity, while the c^{index} distribution range is used to quantify the macrosegregation extremes.

For the columnar solidification benchmark and alloys considered in this study, there exists three mechanisms responsible for the macrosegregation: thermal buoyancy flow, solutal buoyancy flow and species diffusion at the macroscopic scale. By comparison of the two flow mechanisms, the solutal buoyancy overweighs. That is the reason why only the solutal buoyancy force direction is marked in Figs. 1 and 8 (upper raw) indicating the dominant driving force for flow. The impact of thermal and solutal buoyancies on the flow depends on the solidification direction. Therefore, it is not surprising that the final segregation pattern and segregation intensity of each case depend on the alloy and solidification direction, as can be seen in Fig. 8. The diffusion induced macrosegregation falls in a very narrow range, i.e. undetectable in comparison with flow-induced segregation. This result confirms the work of Krane et al. [19]. In the case C3, the dominant solutal buoyancy is against the solidification direction (stabilizing the interdendritic flow), but it cannot (or not possible) fully suppress the thermal buoyancy. Therefore, there still exists a very weak flow, which leads to minor segregation (with the intensity similar to the diffusion-induced surface segregation). If the same color scale,

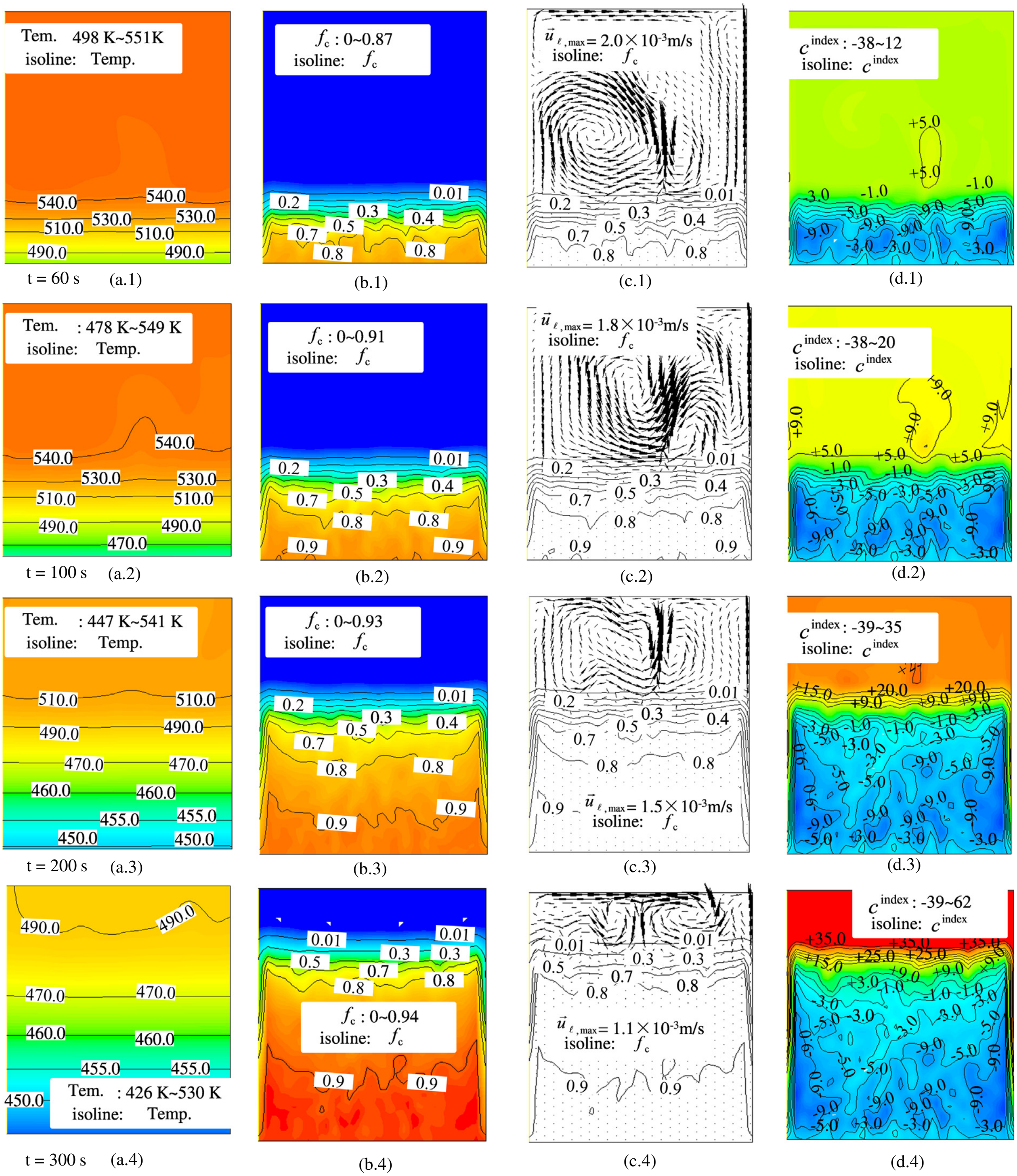

Fig. 5. Solidification sequence of Case C2 at 60, 100, 200 and 300 s. The column a.x shows the evolution of the temperature field in color scale overlaid with isolines; b.x shows contours of f_c in color scale and its isolines, and the columnar tip front position is represented by $f_c = 0.01$; c.x shows the liquid velocity ovelaid with f_c isolines; d.x shows the evolution of macrosegregation (c^{index} in %) in color scale and with isolines. The alloy is Pb-18 wt.%Sn. (For interpretation of the references to color in this figure legend, the reader is referred to the web version of this article.)

e.g. from −100 to +100 of c^{index}, were taken for all 4 cases, no segregation would be seen for the cases C1 and C3. In principle, the solutal convection induced segregation pattern can be estimated according to solutal buoyancy force in respect to the solidification direction, as from the cases C2 and C4.

Can one estimate the macrosegregation tendency based on the simple settings of each case (C1–C4) without performing any calculation? In principle, yes, one can. For example, no segregation or ignorable segregation would occur for C1 and C3; for the case C2, a positive segregation at the top and negative segregation at the bottom; for the case C4, a positive segregation at the bottom and negative segregation at the top. However, fine details of macrosegregation are hard to know. The thermo-solutal convection during solidification is highly transient (Figs. 5–7). Some vortexes evolve while others fall into decay. These transient behaviors of flow (number of vortexes, magnitude and direction of flow, lifetime of each vortex, etc.) determine the fine details of macrosegregation of Fig. 8(b)–(d). For example, in Case 2 and Case 4 the c^{index} distribution in the negative segregation region is not uniform, and some strip like macrosegregation structures are

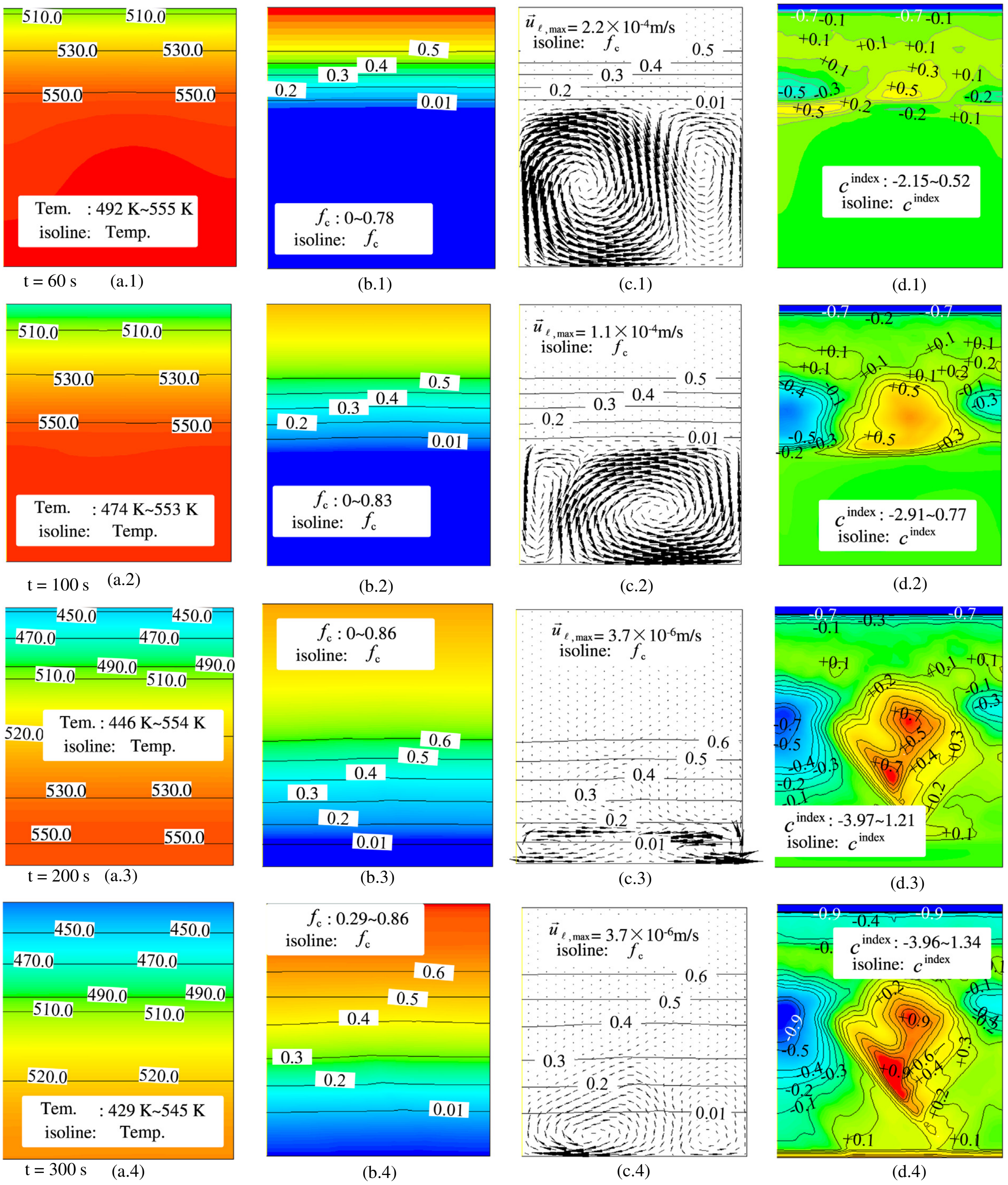

Fig. 6. Solidification sequence of Case C3 at 15, 100, 200 and 300 s. The column a.x shows the evolution of temperature field in color scale overlaid with its isolines; b.x shows contour of f_c in color scale and its isolines; c.x shows the liquid velocity ovelaid with f_c isolines, and the columnar tip front position is represented by $f_c = 0.01$; d.x shows the evolution of macrosegregation (c^{index} in %) in color scale and isolines. The alloy is Pb-18 wt.%Sn. (For interpretation of the references to color in this figure legend, the reader is referred to the web version of this article.)

observed in the negative-to-positive transition zone. In Case 3 there are an irregular shape of positive segregation zone in the middle and two negative segregation zones in both left and right sides of the test casting. The transient behaviours of flow depend not only on the solidification and buoyancy force directions, but also on many other factors such as the mushy zone thickness and morphology, cooling condition and material properties (thermal- and solutal expansion coefficients), etc.

In Case 2 and Case 3, positive segregation channels are predicted along both side boundaries, i.e. symmetry plane (left) and adiabatic wall (right). The flow is confined by the boundaries. The interdendritic melt near the side boundaries is difficult to be brought out of the mushy region, and the solidification is retarded, hence channels form there. This kind of channel segregation was often observed experimentally [52], and it was also predicted numerically by other models [53,54].

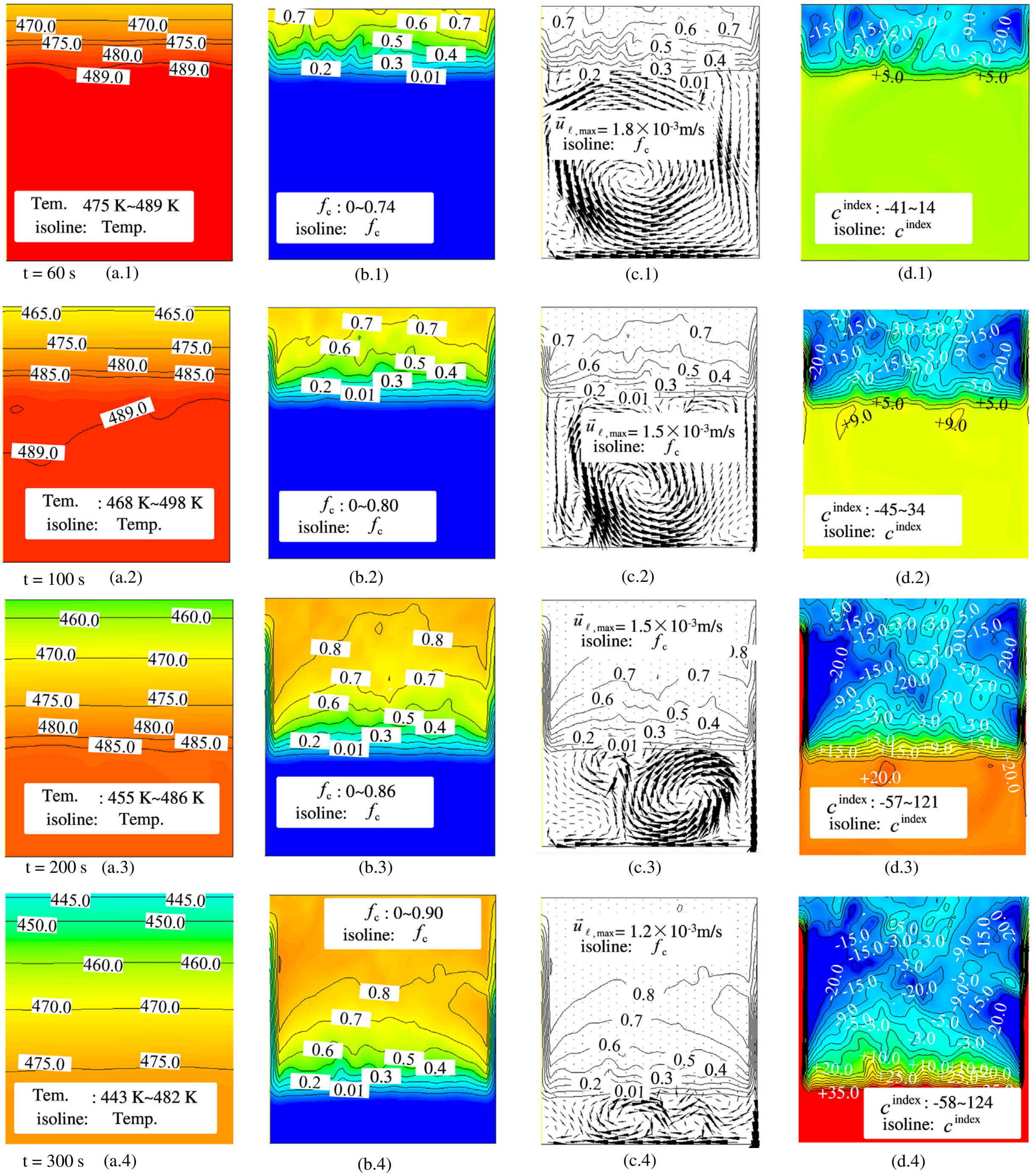

Fig. 7. Solidification sequence of Case C4 at 60, 100, 200 and 300 s. The column a.x shows the evolution of temperature field in color scale overlaid with its isolines; b.x shows contour of f_c in color scale and its isolines, and the columnar tip front position is represented by $f_c = 0.01$; c.x shows the liquid velocity ovelaid with f_c isolines; d.x shows the evolution of macrosegregation (c^{index} in %) in color scale and isolines. The alloy is Sn-10 wt.%Pb. (For interpretation of the references to color in this figure legend, the reader is referred to the web version of this article.)

The macrosegregation intensity (severity) is found to be closely related to the velocity magnitude of the flow. When the velocity is very small ($\sim 10^{-5}$ m/s), the macrosegregation will fall into the same range of diffusion-induced surface segregation, i.e. $|c^{\text{index}}| < 4$ or GMI < 0.1. Case 3 is one example for that. When the velocity magnitude is in the order of 10^{-2} m/s, such as in Case C2 and Case C4, the macrosegregation can reach as high as $|c^{\text{index}}| > 100$ (or GMI > 30).

4.2. Convection-induced macrosegregation

Convection-induced macrosegregation during columnar solidification can be analyzed according to the flow-solidification interaction [55]. It can be described by:

$$\frac{\partial}{\partial t} c_{\text{mix}} = -f_\ell \vec{u}_\ell \cdot \nabla c_\ell. \tag{17}$$

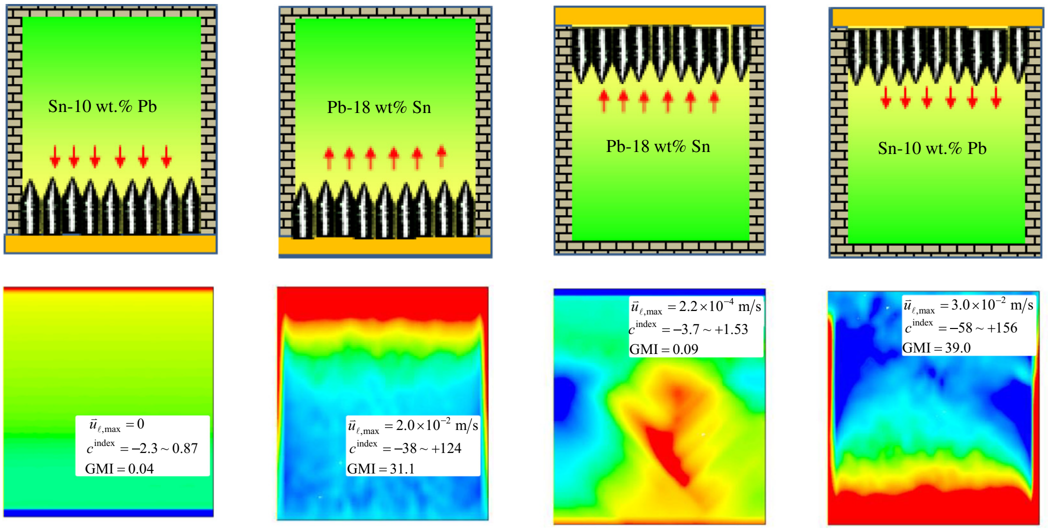

(a) Case C1 (b) Case C2 (c) Case C3 (d) Case C4

Fig. 8. Comparison of the final macrosegregation patterns among 4 cases. The segregation (c^{index} in %) contours are shown in color (low row) with different distribution ranges. The maximum flow velocity during solidification and the global macrosegregation intensity (GMI), are also given. The yellow walls indicate chilled walls, while the hatched ones are adiabatic. (For interpretation of the references to color in this figure legend, the reader is referred to the web version of this article.)

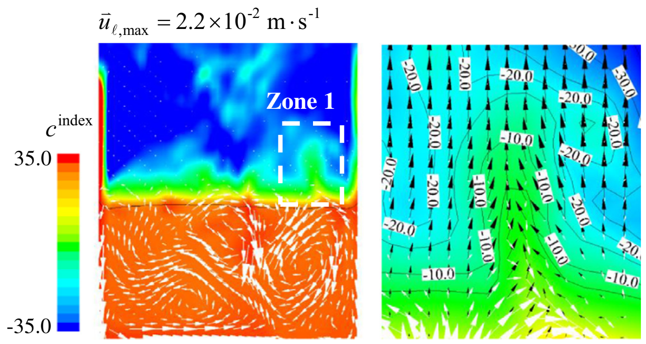

(a) (b)

Fig. 9. Solidification of Case C4 ($t = 50$ s): Sn-10 wt.%Pb cooling from top. (a) Macrosegregation contour (c^{index} in %) overlaid by liquid velocity vectors (white); (b) zoom-in view of Zone 1, where the direction of ∇c_ℓ is also shown by black vectors.

Variation of the local mixture concentration, c_{mix}, is caused by the flow, $\vec{u}_\ell$, of melt in a region where a solute concentration gradient, ∇c_ℓ, exists. In the solidifying mushy zone there exists a strong ∇c_ℓ which points against the solidification direction (for the case of solute partition coefficient k less than 1). According to Eq. (17), an interdendritic flow with its velocity direction pointing towards ∇c_ℓ direction (against the solidification direction) leads to a reduction of c_{mix}, i.e. formation of negative segregation. In another words, a flow against the solidification direction will transport the solute-lean melt to a region to replace the solute-rich melt, hence to cause the reduction of the mixture concentration c_{mix} of the region. Actually the local solidification will accelerate in this scenario. An opposite flow direction, i.e. flow in the solidification direction, leads to formation of positive segregation, and the local solidification will retard. Or to say, the flow in solidification direction will transport the solute-rich melt to a region to replace the solute-lean melt, hence to cause the increase of c_{mix}. Notice that Eq. (17) is derived from the Flemings' theory [56], but it is different from the original one ($\partial c_{\text{mix}}/\partial t = -mf_\ell \vec{u}_\ell \cdot \nabla T$). The current solidification model has considered the diffusion-governed growth kinetics, while the early Flemings' model took a simple microsegregation model based on Gulliver-Scheil assumption (interdendritic melt is infinite mixing). It has been confirmed that the infinite mixing kinetics as assumed by the Gulliver-Scheil or the lever rule, which cannot properly consider the solute distribution in the interdendritic at the early stage of dendrite growth, leads to error estimation of macrosegregation [57,58].

Eq. (17) can be applied to analyze the macrosegregation mechanisms of the current test cases. An example of solidification of Case 4 at 50 s is shown in Fig. 9. Solidification direction is downward. ∇c_ℓ is generally against the solidification direction. The flow is, however, quite transient and dynamic. Just near the solidification front, some flow is following the solidification direction while some flow in other regions is against the solidification direction. Therefore, the c_{mix} distribution at the solidification front is quite non-uniform. As shown in Fig. 9(b), a zoom-in view of a region near the solidification front, the flow $\vec{u}_\ell$ and liquid solute concentration gradient ∇c_ℓ have an opposite direction, leading to formation of a positive segregate. This kind of segregation is sometimes referred to as origin of channel segregation. If the flow keeps in the same direction, i.e. in the solidification direction, the channel will continue to grow and a stable channel will develop. In the current benchmark, no stable channel inside the domain could be seen, because the flow direction changes dynamically.

4.3. Mesh sensitivity

Mesh (grid) size is an important factor influencing the accuracy of segregation calculations. As example, calculations with different mesh size (0.5–2.0 mm) for Case 4 were performed, and the final macrosegregation distributions are compared in Fig. 10. About ¾ of upper region bears negative segregation, about ¼ of the bottom region bears severe positive segregation. The global c^{index} distribution tendencies are almost the same and consistent for all cases of mesh size. In this sense, a relative coarse mesh, e.g. 2 mm, seems to be sufficient to confirm the expectation for the macrosegregation tendency.

In order to perform the quantitative evaluation of the mesh sensitivity, the c^{index} distribution range (segregation extremes $c^{\text{index}}_{\min}$, $c^{\text{index}}_{\max}$) and the global macrosegregation intensity (GMI) are plotted in Fig. 11 against the mesh (grid) size. GMI varies between 30 and

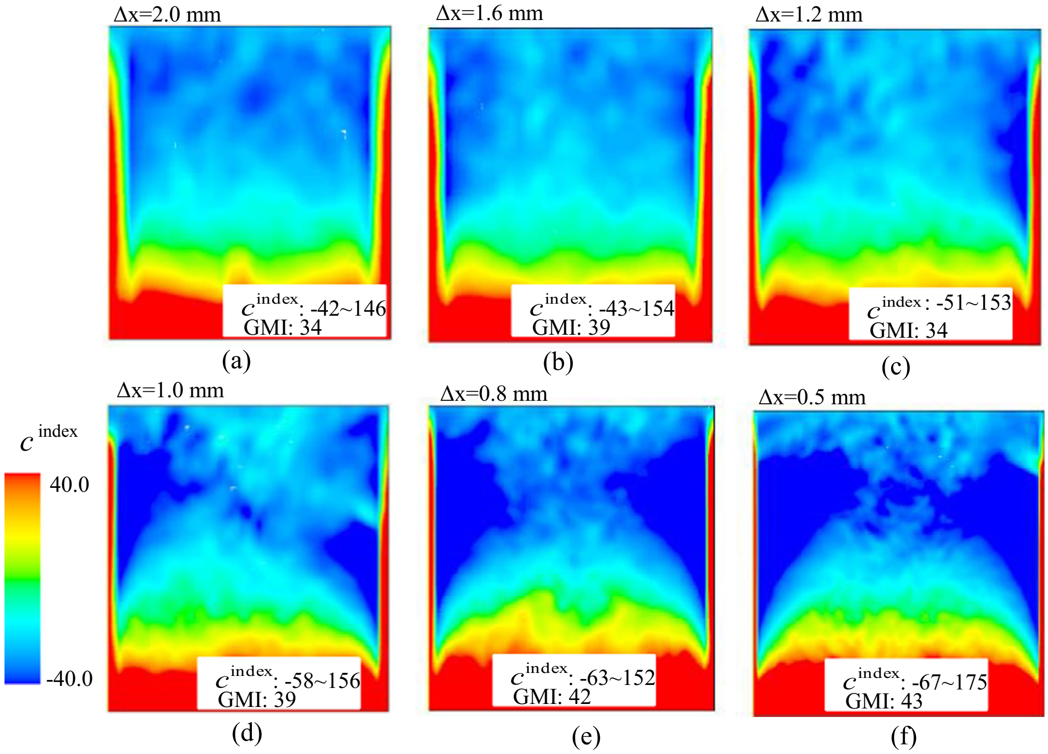

Fig. 10. Mesh sensitivity study of macrosegregation formation in Case C4. The macrosegregation contours (c^{index} in %) are shown in color scale for a mesh size of (a) 2.0 mm, (b) 1.6 mm, (c) 1.2 mm, (d) 1.0 mm, (e) 0.8 mm and (f) 0.5 mm. (For interpretation of the references to color in this figure legend, the reader is referred to the web version of this article.)

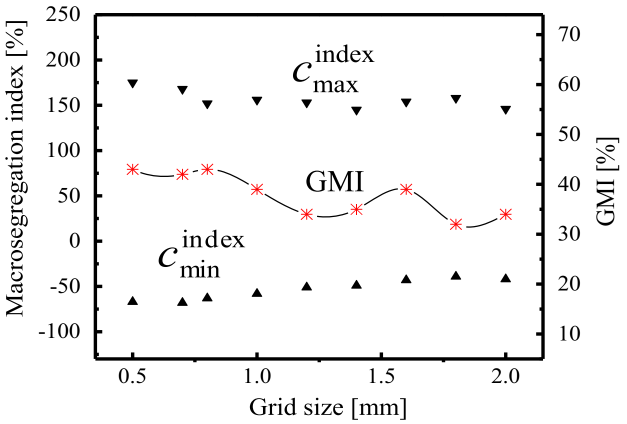

Fig. 11. Influence of mesh size on macrosegregation range (c_{min}^{index}, c_{max}^{index}) and global macrosegregation intensity (GMI) for Case C4.

40% when the mesh size is larger than 1 mm. As the mesh size is reduced to 0.8 mm, the variation range of GMI becomes significantly reduced. However, the c^{index} distribution range varies with the mesh size, even when the mesh size is reduced to as small as 0.5 mm.

From Fig. 10, fine details of the c^{index} distribution show some differences between the calculations of different mesh sizes: one difference is the c^{index} distribution in the negative-to-positive transition zone; one is the thickness of the channels along the side boundaries. The former difference in the fine details of c^{index} distribution is due to the inconsistent flow patterns which are calculated by different mesh sizes. The latter difference in the thickness of segregation channels along the side boundaries is obviously due to insufficient mesh resolution, especially in the boundary layer. The current modelling result shows that the channel thickness is almost linearly reduced with the mesh size. The channel thickness is in the magnitude of one mesh size. According to Kumar et al. [54], who modeled a test casting of the same geometry with an alloy of Sn-5 wt.% Pb as cooled laterally, the channels inside the middle domain of test casting were found to be in the range of 1.0–1.685 mm in thickness and they spanned 2–5 times of mesh sides. The smallest mesh size as used by Kumar et al. is 0.2 mm. The mesh size as used in the current paper is coarser than those as used in [54], but it is smaller than the channel thickness (1.0–1.685 mm) as predicted in [54]. As we discussed in Section 4.1, both side boundaries, i.e. symmetry plane and adiabatic wall, confine the flow. They provide favorite locations for the formation of channel segregates. The channels as formed along boundaries might be much thinner than those inside the middle domain of the test casting. Extreme fine mesh would be necessary to solve the flow in the boundary layer. Further study is needed.

The modelling results presented in previous sections are based on the mesh size of 1 mm. Key features of the predicted segregation patterns of different cases are valid, but the fine details of the c^{index} distribution do not converge to the precise results.

5. Summary

In order to provide exercise examples for metallurgical students to learn different macrosegregation mechanisms, a simple 2D casting with ideal configuration of pure columnar solidification was simulated by using a volume-average based solidification model. 4 test cases were calculated where solidification occur unidirectionally, either upwards or downwards. Two different alloys were considered: Sn-10 wt.%Pb with solute element Pb heavier than the solvent Sn; Pb-18 wt.%Sn with solute element Sn lighter than the solvent Pb. The final macrosegregation tendency in each test case should be estimated without any simulation according to the alloy and the predefined solidification direction. For example, a solute lighter alloy (Pb-18 wt.%Sn) solidifying upwards would lead to a positive segregation (enrichment of Sn) in the top region and negative segregation (poor in Sn) in the bottom region. That is true. However, the modelling results show that more complicated details of macrosegregation distribution can develop due to the complexity of the transient flow.

In the present test cases, 3 macrosegregation mechanisms operate: thermal buoyancy flow, solutal buoyancy flow and macroscopic diffusion in interdendritic melt. Diffusion-induced macrosegregation occurs only at the bottom and top surfaces in an extremely narrow range, and it is ignorable if the mechanism of thermo-solutal buoyancy flow operates. Solutal buoyancy dominates over the thermal buoyancy when both of them operate at the same time. Solidification shrinkage induced macrosegregation, which is also much stronger than the diffusion-induced macrosegregation [19], was not included in the test cases. Details of macrosegregation formation as induced by thermo-solutal convection during columnar solidification can be analyzed by the relation $\partial c_{\mathrm{mix}}/\partial t = -f_\ell \vec{u}_\ell \cdot \nabla c_\ell$.

Calculation of the formation of macrosegregation is sensitive to the mesh size. Although fine details of the c^{index} distribution have not converged to mesh-independent results with the current grid resolution, key features of the global segregation patterns as presented in this paper are valid.

Other 4 cases of equiaxed solidification will be presented as Part II in next paper.

Acknowledgements

The authors acknowledge the financial support from Austrian Research Promotion Agency (FFG) through the project of Bridge Early Stage (No. 842441), as well as the technical support from the industrial partner Primetals Technologies (former Siemens VAI).

References

[1] M.C. Flemings, ISIJ Int. 40 (2000) 833–841.
[2] A. Ludwig, M. Wu, A. Kharicha, Metall. Mater. Trans. A 46A (2015) 4854–4867.
[3] J.A. Dantzig, M. Rappaz, Solidification, EPFL Press, 2009.
[4] A. Ludwig, Lecture note on solidification course in Swiss Federal Institute of Technology of Lausanne (EPFL), Lausanne, 2015.
[5] M.C. Flemings, G.E. Nereo, Trans. Metall. Soc. AIME 239 (1967) 1449–1462.
[6] G. Lesoult, Mater. Sci. Eng. A 413–414 (2005) 19–29.
[7] E.J. Pickering, C. Chesman, S. Al-Bermani, M. Holland, P. Davies, J. Talamantes-Silva, Metall. Mater. Trans. B 46B (2015) 1860–1874.
[8] M. Wu, A. Kharicha, A. Ludwig, Mater. China 34 (2015) 640–651.
[9] C. Beckermann, Int. Mater. Rev. 47 (2002) 243–261.
[10] J. Ni, C. Beckermann, Metall. Mater. Trans. B 22 (1991) 349–361.
[11] A. Ludwig, M. Wu, Metall. Mater. Trans. A 33 (2002) 3673–3683.
[12] M. Wu, A. Ludwig, A. Buhrig-Polaczek, M. Fehlbier, P.R. Sahm, Int. J. Heat Mass Transfer 46 (2003) 2819–2832.
[13] M. Wu, A. Ludwig, J. Luo, Mater. Sci. Forum 475–479 (2005) 2725–2730.
[14] M. Wu, J. Domitner, A. Ludwig, Metall. Mater. Trans. A 43 (2012) 945–964.
[15] H.J. Thevik, A. Mo, Int. J. Heat Mass Transfer 40 (1997) 2055–2065.
[16] H.J. Thevik, A. Mo, T. Rusten, Metall. Mater. Trans. B 30 (1999) 135–142.
[17] M.C. Schneider, C. Beckermann, Int. J. Heat Mass Transfer 38 (1995) 3455–3473.
[18] H.J. Thevik, A. Mo, Metall. Mater. Trans. B 28 (1997) 665–669.
[19] M.J.M. Krane, F.P. Incropera, Metall. Mater. Trans. A 26 (1995) 2329–2339.
[20] W. Bennon, F. Incropera, Int. J. Heat Mass Transfer 30 (1987) 2161–2170.
[21] M.J.M. Krane, F.P. Incropera, D.R. Gaskell, Int. J. Heat Mass Transfer 40 (1997) 3827–3835.
[22] W. Bennon, F. Incropera, Metall. Mater. Trans. B 18 (1987) 611–616.
[23] V. Voller, A. Brent, C. Prakash, Int. J. Heat Mass Transfer 32 (1989) 1719–1731.
[24] M. Schneider, C. Beckermann, Metall. Mater. Trans. A 26 (1995) 2373–2388.
[25] J. Ni, C. Beckermann, Transport Phenomena in Material Processing, vol. 132, ASME HTD, New York, 1990.
[26] C. Beckermann, R. Viskanta, Appl. Mech. Rev. 46 (1993) 1–27.
[27] M. Wu, A. Ludwig, Adv. Eng. Mater. 5 (2003) 62–66.
[28] M. Wu, A. Ludwig, Metall. Mater. Trans. A 37 (2006) 1613–1631.
[29] M. Wu, A. Ludwig, Metall. Mater. Trans. A 38A (2007) 1465–1475.
[30] M. Wu, A. Ludwig, Acta Mater. 57 (2009) 5621–5631.
[31] M. Wu, A. Ludwig, Acta Mater. 57 (2009) 5632–5644.
[32] M. Wu, A. Fjeld, A. Ludwig, Comput. Mater. Sci. 50 (2010) 32–42.
[33] M. Wu, A. Ludwig, A. Fjeld, Comput. Mater. Sci. 50 (2010) 43–58.
[34] J. Li, M. Wu, A. Ludwig, A. Kharicha, Int. J. Heat Mass Transfer 72 (2014) 668–679.
[35] J. Li, M. Wu, J. Hao, A. Kharicha, A. Ludwig, Comput. Mater. Sci. 55 (2012) 419–429.
[36] J. Li, M. Wu, J. Hao, A. Ludwig, Comput. Mater. Sci. 55 (2012) 407–418.
[37] M. Wu, J. Li, A. Ludwig, A. Kharicha, Comput. Mater. Sci. 92 (2014) 267–285.
[38] M. Wu, J. Li, A. Ludwig, A. Kharicha, Comput. Mater. Sci. 79 (2013) 830–840.
[39] N. Leriche, H. Combeau, C.-A. Gandin, M. Založnik, IOP Conf. Series: Mater. Sci. Eng. 84 (2015) 012087.
[40] M. Bellet, H. Combeau, Y. Fautrelle, D. Gobin, M. Rady, E. Arquis, O. Budenkova, B. Dussoubs, Y. Duterrail, A. Kumar, Int. J. Therm. Sci. 48 (2009) 2013–2016.
[41] N. Ahmad, H. Combeau, J.-L. Desbiolles, T. Jalanti, G. Leosoult, J. Rappaz, M. Rappaz, C. Stomp, Metall. Mater. Trans. A 29 (1998) 617–630.
[42] H. Combeau et al., in: A. Ludwig, M. Wu, A. Abdellah (Eds.), Proceedings of 13th Modeling of Casting, Welding and Advanced Solidification Processes, IOP Conf. Series: Mater. Sci. Eng., vol. 33, 2012, http://dx.doi.org/10.1088/1757-899X/33/1/012086.
[43] D.J. Hebditch, J.D. Hunt, Metall. Trans. 5 (1974) 1557–1564.
[44] L. Hachani, K. Zaidat, Y. Fautrelle, Int. J. Heat Mass Transfer 85 (2015) 438–454.
[45] J. Lipton, M.E. Glicksman, W. Kurz, Mater. Sci. Eng. 65 (1984) 57–63.
[46] M.A. Martorano, C. Beckermann, C.A. Gandin, Metall. Mater. Trans. A 34 (2003) 1657–1674.
[47] D. Poirier, Metall. Mater. Trans. B 18 (1987) 245–255.
[48] M. Klassen, J. Cahoon, Metall. Mater. Trans. A 31 (2000) 1343–1352.
[49] J. Gu, C. Beckermann, Metall. Mater. Trans. A 30 (1999) 1357–1366.
[50] E. Cadirli, M. Gündüz, J. Mater. Sci. 35 (2000) 3837–3848.
[51] ANSYS Fluent – Release 14.5, Fluent Theory Guide, ANSYS Inc, <www.ansys.com>.
[52] D. Ma, Q. Wu, A. Bührig-Polaczek, Metall. Mater. Trans. B 43 (2012) 344–353.
[53] J. Guo, C. Beckermann, Numer. Heat Transfer: Part A: Appl. 44 (2003) 559–576.
[54] A. Kumar, B. Dussoubs, M. Zaloznik, H. Combeau, I. Phys. D: Appl. Phys. 42 (2009) 105503.
[55] M. Wu, L. Könözsy, A. Ludwig, W. Schützenhofer, R. Tanzer, Steel Res. Int. 79 (2008) 637–646.
[56] M.C. Flemings, G.E. Nereo, Trans. Met. Soc. AIME 239 (1967) 1449–1461.
[57] M. Zaloznik, H. Combeau, in: S.L. Cockcroft, D.M. Maijer (Eds.), Proceedings of 12th Modeling of Casting, Welding and Advanced Solidification Processes, TMS, 2009, pp. 253–260.
[58] M. Wu, A. Kharicha, A. Ludwig, Mater. Sci. Forum 790–791 (2014) 85–90.